Journal of Materials Chemistry A

PAPER

View Article Online
View Journal | View Issue

Cite this: J. Mater. Chem. A, 2015, 3, 9179

Opto-electronic properties of TiO_2 nanohelices with embedded $HC(NH_2)_2PbI_3$ perovskite solar cells

Jin-Wook Lee,†[a] Seung Hee Lee,†[b] Hyun-Seok Ko,[a] Jeong Kwon,[c] Jong Hyeok Park,[c] Seong Min Kang,[d] Namyoung Ahn,[d] Mansoo Choi,[d] Jong Kyu Kim*[b] and Nam-Gyu Park*[a]

Received 21st September 2014
Accepted 12th November 2014

DOI: 10.1039/c4ta04988h

www.rsc.org/MaterialsA

A $HC(NH_2)_2PbI_3$ solar cell of perovskite structure based on TiO_2 nanohelices has been developed. Well-aligned helical TiO_2 arrays of different pitch (p) and radius (r), helix-1 ($p/2$ = 118 nm, r = 42 nm), helix-2 ($p/2$ = 353 nm, r = 88 nm) and helix-3 ($p/2$ = 468 nm, r = 122 nm), were grown on fluorine-doped tin oxide (FTO) glass by oblique-angle electron beam evaporation. $HC(NH_2)_2PbI_3$ perovskite was deposited on the TiO_2 nanohelices by a two-step dipping method. Helix-1 showed higher short-circuit current density (J_{SC}), whereas helix-3 exhibited slightly higher open-circuit voltage (V_{OC}). $HC(NH_2)_2PbI_3$ perovskite combined with helix-1 demonstrated an average power conversion efficiency of 12.03 ± 0.07% due to its higher J_{SC} compared to helix-2 and helix-3. The higher J_{SC} of helix-1 could be attributed to its greater light scattering efficiency and higher absorbed photon-to-current conversion efficiency. In addition, despite having the longest pathway structure, helix-1 showed rapid electron diffusion, attributed to its higher charge injection efficiency due to the larger contact area between perovskite and TiO_2. We have established that fine tuning of the interface between perovskite and the electron-injecting oxide is a crucial factor in achieving a perovskite solar cell of high performance.

Introduction

An initial report of organo-lead halide perovskite as a light harvester,[1] following reports of a perovskite-sensitized solar cell of 6.5% efficiency[2] and 10–11% long-term durable solid-state perovskite solar cells,[3,4] has over recent years triggered intensive interest in perovskite solar cells. As a result, rapid improvements in power conversion efficiency (PCE) have been demonstrated by optimizing the device structure and deposition process,[5–10] and a PCE as high as 19.3% has been demonstrated using a planar structure, and a PCE of 17.9% obtained from a mesoscopic structure.[8,10]

Along with efforts to enhance photovoltaic performance, studies aimed at the improved understanding of the origin of the superb performance of the perovskite solar cell have been carried out. Methylammonium lead iodide (MALI) was found to have the ability to accumulate charges and to transfer electrons and holes;[11–13] diffusion lengths for electrons and holes were estimated to be over 1 μm.[12,13] These unique properties of organometal halide perovskites have changed its diverse device structure from a sensitization concept to a planar p–n junction concept.[14] Although the diffusion length of charges in perovskite are found to be much greater than its absorption depth, represented by the reciprocal of its absorption coefficient,[15,16] it remains arguable whether or not an electron-accepting network for charge separation, such as mesoscopic TiO_2, in the perovskite layer is necessarily required. Some studies have been conducted to gauge the effect of different n-type electron-accepting materials with various morphologies, including ZnO nanorods, ZnO nanoparticles, rutile TiO_2 nanoparticles and TiO_2 nanorods.[17–20] Regardless of the materials used, it has been found that an electron acceptor in a perovskite solar cell plays an important role in improving its photovoltaic performance. Regarding charge collection, TiO_2 nanorods are promising candidates, since better charge transport is expected through a 1-dimensional pathway than a 3-dimensional porous nanoparticle network. ZnO nanorods are found to be more efficient for charge collection than TiO_2 nanorods, due to more rapid charge carrying.[18] In addition, electron injection behavior has been found to differ with the crystal phase, in which more electrons were injected into rutile than anatase TiO_2, and this consequently affected the photovoltaic performance of the perovskite solar cell.[19]

Recently, formamidinium-based perovskite, $HC(NH_2)_2PbI_3$ (FALI), has been reported to be an acceptable alternative to the methylammonium analogue.[21–26] Compared to MALI, FALI is

[a]School of Chemical Engineering and Department of Energy Science, Sungkyunkwan University, 440-746, Suwon, Korea. E-mail: npark@skku.edu

[b]Department of Materials Science and Engineering, Pohang University of Science and Technology, 790-784, Pohang, Korea. E-mail: kimjk@postech.ac.kr

[c]School of Chemical Engineering, Sungkyunkwan University, Suwon 440-746, Korea

[d]Department of Mechanical and Aerospace Engineering, Seoul National University, Seoul 151-742, Korea

† These authors contributed equally to the study.

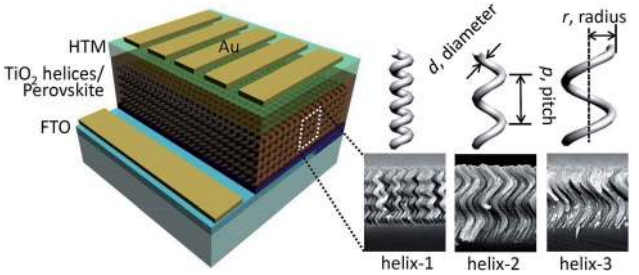

Fig. 1 Schematic description of the perovskite solar cell, consisting of TiO_2 helices and $HC(NH_2)_2PbI_3$ (perovskite). Cross-sectional SEM images of three different TiO_2 helices, helix-1, helix-2 and helix-3, grown on silicon wafer are also shown.

free from phase transitions and is relatively photo-stable, and it has a wider absorption range.[21,26] In addition, a mesoporous TiO_2 layer embedded in the FALI layer has been found to improve charge collection and fill factor by lowering series resistance and increasing shunt resistance.[26] Since charge transport and collection are influenced by oxide type and phase, as is observed in methylammonium lead iodide perovskite solar cells,[18,19] we were stimulated to investigate the effect of 1-dimensional TiO_2 nanorods in the FALI system. It was also of interest to examine the effect of electron transport and collection on 1-dimensional TiO_2 nanorods of different pathway lengths.

We can now report the results based on the opto-electronic properties of TiO_2 helix-embedded FALI perovskite solar cells. Highly aligned helical TiO_2 arrays were deposited on FTO glass by oblique-angle deposition, which is a very promising method for producing aligned nanostructural films with excellent shape control.[27] Arrays of 400 nm-thick helical TiO_2 of differing radius, pitch and turn were used as an electron-accepting network in a FALI-perovskite solar cell. Morphological tuning of helical TiO_2 resulted in an increase in charge collection and light harvesting efficiency. Using TiO_2 nanohelices of 118 nm half-pitch and 42 nm radius, a PCE of 12.03% was demonstrated under AM 1.5G one-sun illumination.

Methods

Deposition of TiO_2 nanohelices

FTO glass was cleaned using UV-ozone for 15 min and washed with a detergent solution. The substrates were further cleaned in an ethanol bath under sonication. A dense TiO_2 blocking layer was formed by spin-coating 0.15 M titanium diisopropoxide bis(acetylacetonate) (Aldrich, 75 wt% in isopropanol) solution onto the cleaned FTO glass and annealing at 500 °C for 15 min. Arrays of 400 nm-thick helical TiO_2 films of different shapes were formed on the FTO glass by an oblique-angle deposition technique using an electron-beam evaporator. With oblique-angle deposition, by adjusting the deposition conditions, such as substrate tilt angle, substrate rotation speed, time interval between substrate rotation, and deposition rate, a variety of three-dimensional nanostructures, including nanohelices, slanted nanorods, and nano zig-zags, were produced with precise control of geometrical shape. At the initial stage of the oblique-angle deposition, a TiO_2 vapor flux with a high substrate tilt angle formed small islands of TiO_2, producing self-shadowed regions.[27–29] Limited atom diffusion into the self-shadowed regions, and preferential deposition of the TiO_2 vapor flux in the non-shadowed area, created porous thin films with a variety of nanostructures, depending on the deposition conditions. Helical TiO_2 nanostructures could be produced by rotating the substrate at controlled time intervals at a high substrate tilt angle.

Three samples, helix-1, helix-2 and helix-3, were produced using an identical substrate tilt angle of 80°, at a film deposition rate of 5 Å s^{-1} and a substrate rotational speed of 2 s, but with different time intervals between substrate rotations of 6, 12, or 24 s, respectively, in order to form TiO_2 helices of different geometrical shapes. The average helical TiO_2 diameter of each sample was estimated to be 66.4 ± 3.5 nm by SEM imaging. The pitch of the helical TiO_2 became longer with increasing time

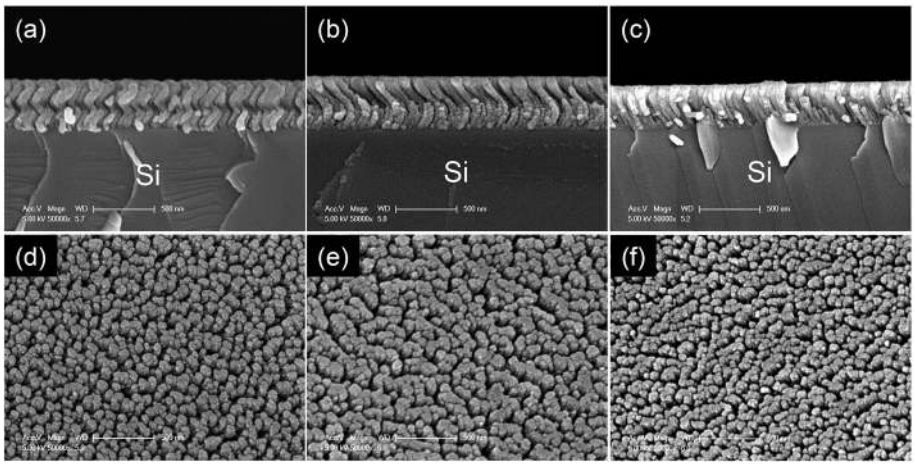

Fig. 2 Cross-sectional and surface SEM images of (a) and (d) helix-1, (b) and (e) helix-2 and (c) and (f) helix-3, grown on a silicon wafer. The scale bars represent 500 μm.

Table 1 Geometric parameters, pitch (p), turns, radius (r) diameter (d) and length (l), of the TiO_2 nanohelices

TiO_2 nanohelices	$p/2$	Turns	r	d	l ($p \times$ turns)
Helix-1	118 nm	1.7	42 nm	66.4 ± 3.5 nm	401.2 nm
Helix-2	353 nm	0.57	88 nm		402.4 nm
Helix-3	468 nm	0.43	122 nm		402.5 nm

interval, due to greater deposition along one direction of the helix. The thickness of each sample was precisely controlled using experimentally acquired tooling factors (deposited film thickness on sample/deposited film thickness on an alloy quartz crystal microbalance sensor) for each set of deposition conditions: 0.72, 0.79 and 1.02 for helix-1, helix-2 and helix-3, respectively. In order to improve the crystallinity of the helical TiO_2, samples were annealed at 500 °C for 30 min under ambient air conditions. Helical TiO_2 films were post-treated with $TiCl_4$ (Aldrich, >98%) by dipping in a 20 mM aqueous $TiCl_4$ solution at 70 °C for 10 min, followed by heat treatment at 500 °C for 30 min.

Production of FALI perovskite solar cells

$HC(NH_2)_2I$ was synthesized according to the method described elsewhere.[26] FALI was deposited on an FTO substrate with TiO_2 nanohelices by a two-step dipping technique. 1 M PbI_2 (Aldrich, 99%) in *N*,*N*-dimethylformamide (Sigma-Aldrich, 99.8%) solution was spin-coated at 6000 rpm for 25 s. The PbI_2-coated helical TiO_2 film was dried at 40 °C for 3 min, followed by 10 min at 100 °C. The film was then dipped in 10 mg mL^{-1} $HC(NH_2)_2I$ in isopropanol (Sigma-Aldrich, 99.5%) solution for 1 min. The electrode was spun at 500 rpm for 5 s, 1500 rpm for 10 s, and 3000 rpm for 20 s to ensure uniform drying, followed by heating in turn for 3 min at 40 °C and 15 min at 150 °C. The electrode was then washed with isopropanol for 15 s to remove unreacted $HC(NH_2)_2I$, and dried 5 min at 150 °C. A solution of 72.3 mg 2,2′7,7′-tetrakis-(*N*,*N*-di-*p*-methoxyphenylamine)-9,9′-*spiro*-bifluorene(*spiro*-MeOTAD) was prepared in 1 mL chlorobenzene, with 28.8 μL 4-*tert*-butyl pyridine and 17.5 μL lithium bis(trifluoromethanesulfonyl)imide solution (520 mg in 1 mL acetonitrile (Sigma-Aldrich, 99.8%)) as additives. The *spiro*-MeOTAD solution was spin-coated on the FALI layer at 4000 rpm for 20 s. Gold was thermally evaporated at 1 Å s^{-1} and used as the positive electrode.

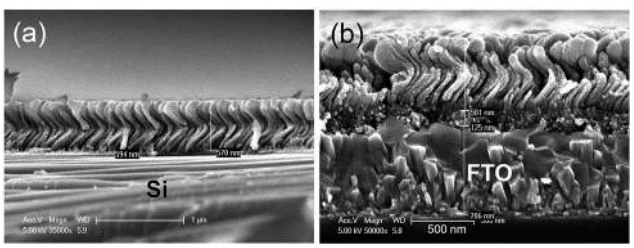

Fig. 3 Helical TiO_2 from the same batch, (a) deposited on silicon wafer, and (b) a compact TiO_2 underlayer coated on FTO glass (TEC-8).

Characterization

Current density and voltage curves were recorded using a Keithley 2400 source meter under AM 1.5G one-sun illumination (100 mW cm^{-2}) provided by a solar simulator (Oriel Sol 3A class AAA). A 450 W Xenon lamp (Newport 6279NS) was used as a light source. The light intensity was adjusted using a NREL-calibrated Si solar cell equipped with KG-2 filter. During the measurement the device was covered with a metal aperture mask of area 0.123 cm^2. External quantum efficiency (EQE, also known as incident photon-to-current efficiency, IPCE) was measured using a specially designed system (PV Measurement Inc., Boulder, CO). A 75 W Xenon lamp (Ushio, Japan) was used as a monochromatic light source, and EQE was measured in DC mode without bias light. Time-limited photocurrent response was monitored using a 550 nm monochromatic beam in which the beam was divided into different frequencies. Cross-sectional morphologies of the TiO_2 helices were investigated using a high-resolution scanning electron microscopy (SEM; JSM-7600F, JEOL) and a focused ion-beam SEM (FIB-SEM, Zeiss Auriga). Time constants for electron transport were determined using the transient photocurrent measurement setup described elsewhere,[30] in which a weak laser pulse at 532 nm superimposed on a relatively large bias illumination at 680 nm was used to generate the pulsed photocurrent.

Results and discussion

Fig. 1 shows schematically the structure of the perovskite solar cell, consisting of TiO_2 helices and FALI perovskite, in which three different geometrical shapes of helical TiO_2, helix-1, helix-2 and helix-3, formed by an oblique-angle deposition method, were investigated. The helical structure can be defined in terms of the pitch of the helix (p), its radius (r), and the diameter of the helical cylinder (d), as illustrated in Fig. 1.

Fig. 2(a)–(f) show cross-sectional and surface SEM images of the arrays of helical TiO_2 nanostructured thin films, helix-1, helix-2 and helix-3, grown on a Si substrate at time intervals of 6, 12 and 24 s, respectively. The geometrical parameters measured are summarized in Table 1.

A longer time interval provided more time for the vapor flux to be deposited in one direction, resulting in a longer pitch of the helical TiO_2, while the number of turns decreased for a similar film thickness. The porosity of the helix-2 thin film was estimated to be ~63% by a linear effective medium approximation of refractive index value, measured using ellipsometry. The three types of nanohelices were grown at different time intervals between substrate rotations, but an identical substrate-tilt angle (80°). The porosity of the three types of TiO_2

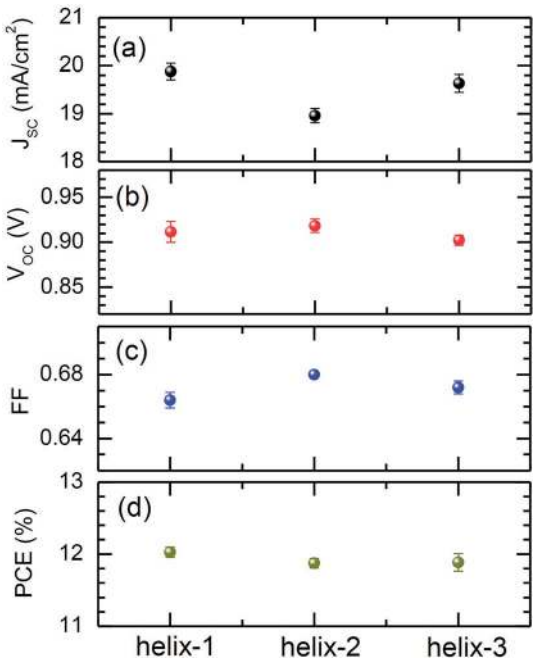

Fig. 4 (a) Short-circuit current density (J_{SC}), (b) open-circuit voltage (V_{OC}), (c) fill factor (FF) and (d) power conversion efficiency (PCE) of $HC(NH_2)_2PbI_3$ perovskite solar cells based on TiO_2 nanohelices. The error bar represents the standard deviation. The data were collected from five cells.

helices was therefore expected to be similar, since the porosity of the nanocolumns grown using oblique-angle deposition depended on the angle of incident vapor flux (substrate-tilt angle).[31] Such high porosity values confirmed the presence of a high density of pores, into which the perovskite could easily penetrate during the two-step dipping procedure.[32] The microstructural evolution of helical TiO_2 by thermal annealing has been described in a previous paper.[33] The amorphous phase TiO_2 deposited was transformed into a highly crystalline anatase phase during thermal annealing at 500 °C for 30 min, which should provide an effective pathway for electron transportation due to the probable removal of trap states.[32] The average grain size along the growth axis of helix has been shown in a previous study to be 413 ± 25 nm, and was much larger than the widely used TiO_2 nanoparticles (20–60 nm).[33] Electrodes based on TiO_2 nanohelices can therefore be expected to show better electron transport properties than those based on nanoparticles.

To ensure that the techniques and conditions for growing the helical TiO_2 on a silicon wafer were applicable to a FTO substrate with haze, the helical TiO_2 layers in the same batch grown, respectively, on silicon wafer and FTO glass were compared. Since a compact thin TiO_2 underlayer coated on FTO was required for the perovskite solar cell, helical TiO_2 was grown on the compact TiO_2 layer at a thickness of 40 nm. As can be seen in Fig. 3, no significant difference either in thickness or morphology was detected, confirming that the procedure for growth of helical TiO_2 was equally applicable to both silicon wafer and FTO glass.

Fig. 4 compares the photovoltaic parameters of helical TiO_2-based perovskite solar cells, the parameters measured being summarized in Table 2. Compared to helix-2, helix-1 and helix-3 showed 4.9% and 3.6% higher short-circuit current density (J_{SC}), respectively. Compared to J_{SC}, the differences in V_{OC} and FF were not significant, although on average helix-2 showed slightly higher V_{OC} and FF. As a result, helix-1 had the highest PCE, mainly due to having the highest J_{SC}. Opto-electronic properties were further investigated using helix morphology in order to understand the basis for the difference in J_{SC}, by means of light harvesting efficiency (LHE), EQE, absorbed photon-to-current conversion efficiency (APCE), and the transient photocurrent response.

Optical properties are evaluated in Fig. 5 to explain the basis for the differences in J_{SC}. LHE was calculated from the reflectance and transmittance of the films (Fig. 5(a)) by means of eqn (1):[18]

$$\mathrm{LHE} = (1 - R)\,(1 - 10^{-A}), \quad (1)$$

where R is the reflectance and A the absorbance of the film. As can be seen in Fig. 5(b), helix-1 showed slightly higher LHE over the wavelengths between 550 nm and 800 nm, helix-2 showed the lowest LHE, and helix-3 was intermediate. The higher LHE of helix-1 probably resulted from greater scattering, particularly at longer wavelengths, due to increased diffuse reflectance.

The surface area of helical TiO_2 was calculated by designing a 3D model of a helix using the 3D MAX program, based on the parameter measurements in Table 1, in which the ratios of surface area of helix-1 : helix-2 : helix-3 were calculated to be 1.17 : 1.00 : 1.08. Since light scattering occurs in inhomogeneous optical media, in other words at the interface between two media of different reflective indices, it is reasonable that the interface of helical TiO_2 and FALI perovskite should act as a scattering center. Thus, a helical TiO_2 film of higher surface area could be expected to produce a greater increase in LHE due to higher light scattering than that of TiO_2 nanohelices of low surface area.

Table 2 The short-circuit current density (J_{SC}), open-circuit voltage (V_{OC}), fill factor (FF) and power conversion efficiency (PCE) of TiO_2 helices embedded with $HC(NH_2)_2PbI_3$ perovskite solar cells at AM 1.5G one-sun illumination (100 mW cm^{-2}). The data were collected from five cells

TiO_2 nanohelices	J_{SC} (mA cm^{-2})	V_{OC} (V)	FF	PCE (%)
Helix-1	19.88 ± 0.17	0.912 ± 0.012	0.66 ± 0.00	12.03 ± 0.07
Helix-2	18.96 ± 0.15	0.918 ± 0.008	0.68 ± 0.00	11.87 ± 0.07
Helix-3	19.64 ± 0.19	0.902 ± 0.006	0.67 ± 0.00	11.88 ± 0.12

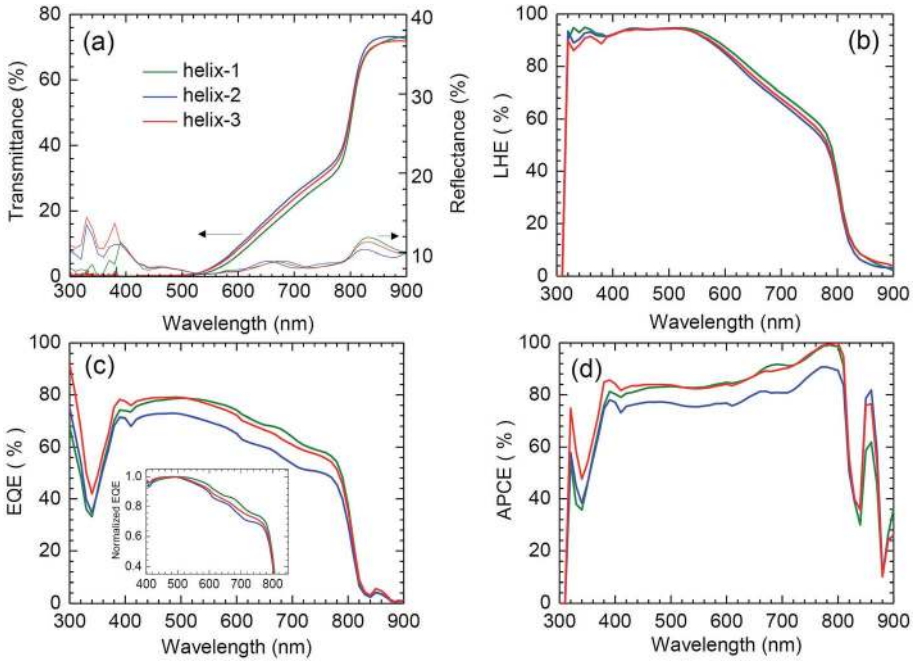

Fig. 5 (a) Transmittance and reflectance, and (b) light harvesting efficiency (LHE) of the TiO_2/$HC(NH_2)_2PbI_3$/*spiro*-MeOTAD film incorporating different helix structures; (c) external quantum efficiency (EQE) and (d) adsorbed photon-to-electron conversion efficiency of a $HC(NH_2)_2PbI_3$ perovskite solar cell based on helical TiO_2.

In the EQE spectra (Fig. 5(c)), integrated values of J_{SC} were calculated to be 19.24 mA cm^{-2} for helix-1, 17.09 mA cm^{-2} for helix-2 and 19.00 mA cm^{-2} for helix-3, in good agreement with the trend in the determined values of J_{SC} shown in Table 1. The inset in Fig. 5(c) shows normalized EQE spectra. The overall tendency of the normalized EQE spectra for wavelengths ranging from 550 nm to 800 nm was well matched with the LHE results, which means that the increased J_{SC} in helix-1 and helix-3 compared to helix-2 was partially attributable to the increase in LHE due to light scattering. APCE was calculated from LHE and EQE using eqn (2):[18]

$$\text{APCE (\%)} = \text{EQE (\%)}/\text{LHE (\%)} \quad (2)$$

Plots of APCE spectra are shown in Fig. 5(d), in which helix-1 and helix-3 were estimated to be 8% higher than that of helix-2 over the whole wavelength region, in line with eqn (3):[34]

$$\text{APCE} = \varphi_{inj} \times \varphi_{coll}, \quad (3)$$

in which φ_{inj} and φ_{coll} are electron injection and collection efficiency, respectively. The low APCE is likely to be attributable either to low charge injection or low collection efficiency, or both. This indicates that charge injection and/or charge

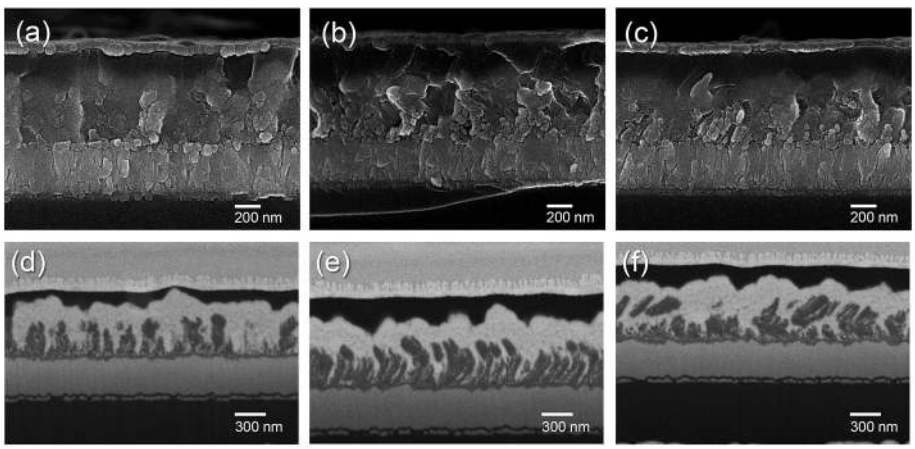

Fig. 6 (a)–(c) Cross-sectional SEM images, and (d)–(f) FIB-assisted SEM images, for perovskite solar cells for (a) and (d) helix-1, (b) and (e) helix-2 and (c) and (f) helix-3.

collection are probably affected by morphological differences in the TiO_2 nanohelices.

Fig. 6 shows cross-sectional SEM images, together with FIB-assisted SEM images, for FALI perovskite solar cells of different helical TiO_2 structures. It was difficult to distinguish helical TiO_2 and the infiltrated FALI perovskite from normal SEM images. However, each component is clearly identified in the FIB-assisted SEM images (Fig. 6(d)–(f)), in which perovskite was fully integrated into *ca.* 400 nm thick helical TiO_2 films, and a *ca.* 200 nm thick capping layer was additionally formed. In the vicinity of the interface between the TiO_2 nanohelices and FALI, there was opportunity for electron injection from FALI to TiO_2.

In Fig. 7 the time-limited photocurrent response of different helical TiO_2 nanostructures is compared. With light chopped at 4 Hz and 10 Hz, helix-1 showed the most rapid photocurrent response, helix-2 gave the slowest response, and helix-3 was intermediate. This emphasized that charge collection in the perovskite solar cell with helix-2 was less efficient compared to the others. This correlated well with photovoltaic performance and APCE. With the incident light chopped at 50 Hz, the overall intensity of the photocurrent response decreased due to the limited response of electrons in TiO_2,[35] and certain rapidly responding components were identified (Fig. 7(c)). These components were probably due to charge transport through the perovskite layer itself, bearing in mind the much higher diffusion coefficient of electrons in perovskite (0.036 $cm^2\ s^{-1}$) than in TiO_2 (6×10^{-5} $cm^2\ s^{-1}$).[19] The amplitude of the rapidly responding components increased in the order, helix-2, helix-3 and helix-1, which is the reverse order to surface area. With a larger surface area, a higher portion of the electrons generated in perovskite are regarded as injected into the TiO_2 network, a portion of electrons transported through the perovskite layer are assumed to be decreased, and *vice versa*.

The time constants for electron transport (τ_c) of the FALI perovskite solar cells incorporating different helical TiO_2 structures are compared in Fig. 8. τ_cs was determined as 8.70×10^{-5} s for helix-1, 2.36×10^{-4} s for helix-2, and 1.39×10^{-4} s for helix-3. The corresponding diffusion coefficients were calculated as 7.83×10^{-6} $cm^2\ s^{-1}$, 2.88×10^{-6} $cm^2\ s^{-1}$, and 4.90×10^{-6} $cm^2\ s^{-1}$, respectively, corresponding to the electron transport in helical TiO_2. Contrary to our expectation that electron transport would be restricted by short pitch with high turns such as in helix-1, under the assumption that all the electrons were injected, electron transport was more rapid in the sequence, helix-1, helix-3, and helix-2. The difference in diffusion coefficient was probably related to the different quantity of electrons injected into TiO_2. Indeed, the different

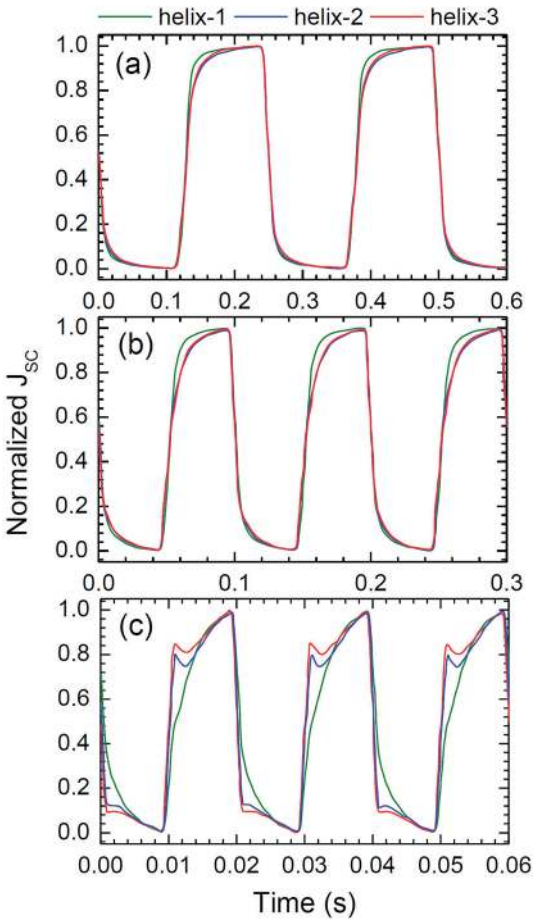

Fig. 7 Time-limited photocurrent response of $HC(NH_2)_2PbI_3$ perovskite solar cells depending on TiO_2 nanohelices, at different chopping frequencies, (a) 4 Hz, (b) 10 Hz, and (c) 50 Hz. A 530 nm monochromatic beam generated from a 75 W xenon lamp was used as light source.

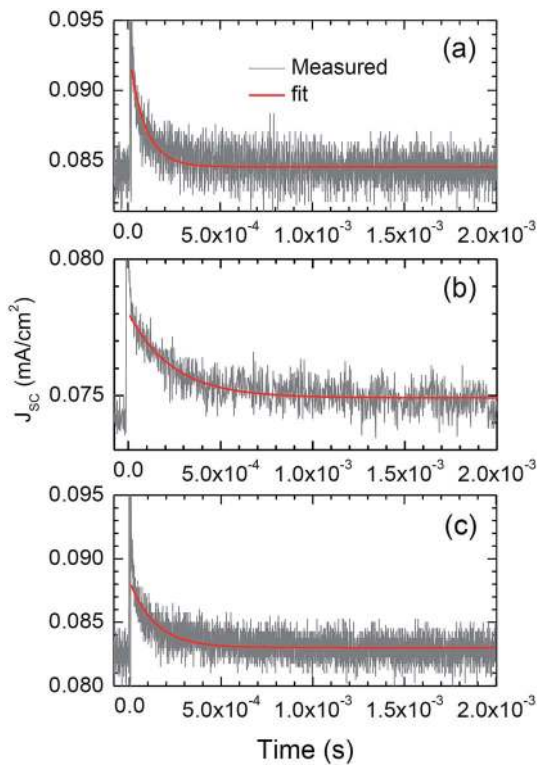

Fig. 8 Transient photocurrent decay measurement of the $HC(NH_2)_2PbI_3$ perovskite solar cells based on (a) helix-1, (b) helix-2, and (c) helix-3. A 670 nm monochromatic beam was used as bias light, superimposed on a 532 nm monochromatic laser pulse.

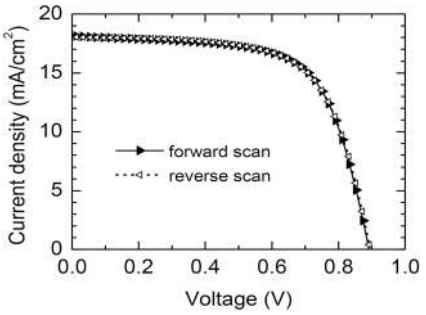

Fig. 9 Current density–voltage curves of a $HC(NH_2)_2PbI_3$ perovskite solar cell based on TiO_2 nanohelix (helix-3), depending on scan direction.

magnitude of bias current density at a given light intensity was an indication of different photo-charge density in TiO_2, resulting in a difference in electron diffusion coefficient.[36] When considering the length of the electron pathway, helix-1 is expected to have the lowest electron diffusion coefficient. However, helix-1 had the highest electron diffusion coefficient, which means that the length of electron pathway was not the dominant factor, but that charge injection efficiency from FALI to TiO_2 in fact determined the electron transport rate in this system. Therefore, the higher J_{SC} from helix-1 may be attributed to higher charge injection efficiency, despite the longer pathway compared to the shortest pathway and lower J_{SC} of helix-2.

Finally, we investigated the hysteresis effect of a $HC(NH_2)_2PbI_3$ perovskite solar cell based on TiO_2 nanohelices. As can be seen in Fig. 9, no difference in current density–voltage curves between forward (from J_{SC} to V_{OC}) and reverse (from V_{OC} to J_{SC}) scanning modes could be observed. This indicated that nanohelix-embedded $HC(NH_2)_2PbI_3$ was free from hysteresis. Nanohelical TiO_2 plays an important role in the suppression of hysteresis, since the capacitive charges are likely to be quickly dissipated by charge separation in the presence of nanohelices.[37]

Conclusions

The following conclusions may be drawn:

(1) The geometrical shape of the helical TiO_2 had no significant effect on electron transport in TiO_2.

(2) An increase in perovskite/TiO_2 contact area by increasing the surface area of the oxide film was found to increase light harvesting and charge injection.

(3) An increase in electron injection from perovskite to TiO_2 led to more rapid electron diffusion in TiO_2, regardless of the pathway structure.

This indicated that the contact area between TiO_2 and FALI perovskite was critical, and fine tuning of interface between perovskite and electron-injecting oxide therefore became a crucial factor in achieving a high performance perovskite solar cell.

Acknowledgements

This study was supported by National Research Foundation of Korea (NRF) grants funded by the Ministry of Science, ICT and Future Planning (MSIP) of Korea, under contracts NRF-2010-0014992, NRF-2012M1A2A2671721, NRF-2012M3A7B4049986 (Nano Material Technology Development Program), NRF-2012M3A6A7054861 (Global Frontier R&D Program on the Center for Multiscale Energy System), and 2011-220-D00064 (Global Research Network program), and also by the POSCO Fusion Technology Center for Materials.

References

1 A. Kojima, K. Teshima, Y. Shirai and T. Miyasaka, *J. Am. Chem. Soc.*, 2009, **131**, 6050–6051.
2 J.-H. Im, C.-R. Lee, J.-W. Lee, S.-W. Park and N.-G. Park, *Nanoscale*, 2011, **3**, 4088–4093.
3 H.-S. Kim, C.-R. Lee, J.-H. Im, K.-B. Lee, T. Moehl, A. Marchioro, S.-J. Moon, R. Humphry-Baker, J.-H. Yum, J. E. Moser, M. Grätzel and N.-G. Park, *Sci. Rep.*, 2012, **2**, 591.
4 M. M. Lee, J. Teuscher, T. Miyasaka, T. N. Murakami and H. J. Snaith, *Science*, 2012, **338**, 643–647.
5 J. Burschka, N. Pellet, S.-J. Moon, R. Humphry-Baker, P. Gao1, M. K. Nazeeruddin and M. Grätzel, *Nature*, 2013, **499**, 316–319.
6 M. Liu, M. B. Johnston and H. J. Snaith, *Nature*, 2013, **501**, 395–398.
7 N. J. Jeon, J. H. Noh, Y. C. Kim, W. S. Yang, S. Ryu and S. I. Seok, *Nat. Mater.*, 2014, **13**, 897–903.
8 H. Zhou, Q. Chen, G. Li, S. Luo, T.-b. Song, H.-S. Duan, Z. Hong, J. You, Y. Liu and Y. Yang, *Science*, 2014, **345**, 542–546.
9 J.-H. Im, I.-H. Jang, N. Pellet, M. Gratzel and N.-G. Park, *Nat. Nanotechnol.*, 2014, **9**, 927–932.
10 Research Cell Efficiency Records, NREL, http://www.nrel.gov/ncpv/.
11 H.-S. Kim, I. Mora-Sero, V. Gonzalez-Pedro, F. Fabregat-Santiago, E. J. Juarez-Perez, N.-G. Park and J. Bisquert, *Nat. Commun.*, 2013, **4**, 2242.
12 S. D. Stranks, G. E. Eperon, G. Grancini, C. Menelaou, M. J. P. Alcocer, T. Leijtens, L. M. Herz, A. Petrozza and H. J. Snaith, *Science*, 2013, **342**, 341–344.
13 G. Xing, N. Mathews, S. Sun, S. S. Lim, Y. M. Lam, M. Grätzel, S. Mhaisalkar and T. C. Sum, *Science*, 2013, **342**, 344–347.
14 H.-S. Kim, S. H. Im and N.-G. Park, *J. Phys. Chem. C*, 2014, **118**, 5615–5625.
15 J.-H. Im, C.-R. Lee, J.-W. Lee, S.-W. Park and N.-G. Park, *Nanoscale*, 2011, **3**, 4088–4093.
16 N.-G. Park, *J. Phys. Chem. Lett.*, 2013, **4**, 2423–2429.
17 K. Mahmood, B. S. Swain and H. S. Jung, *Nanoscale*, 2014, **6**, 9127–9138.
18 D.-Y. Son, J.-H. Im, H.-S. Kim and N.-G. Park, *J. Phys. Chem. C*, 2014, **118**, 16567–16573.
19 J.-W. Lee, T.-Y. Lee, P. J. Yoo, M. Grätzel, S. Mhaisalkard and N.-G. Park, *J. Mater. Chem. A*, 2014, **2**, 9251–9259.
20 H.-S. Kim, J.-W. Lee, N. Yantara, P. P. Boix, S. A. Kulkarni, S. Mhaisalkar, M. Grätzel and N.-G. Park, *Nano Lett.*, 2013, **13**, 2412–2417.
21 C. C. Stoumpos, C. D. Malliakas and M. G. Kanatzidis, *Inorg. Chem.*, 2013, **52**, 9019–9038.

22 T. M. Koh, K. Fu, Y. Fang, S. Chen, T. C. Sum, N. Mathews, S. G. Mhaisalkar, P. P. Boix and T. Baikie, *J. Phys. Chem. C*, 2014, **118**, 16458–16462.
23 G. E. Eperon, S. D. Stranks, C. Menelaou, M. B. Johnston, L. M. Herz and H. J. Snaith, *Energy Environ. Sci.*, 2014, **7**, 982–988.
24 S. Pang, H. Hu, J. Zhang, S. Lv, Y. Yu, F. Wei, T. Qin, H. Xu, Z. Liu and G. Cui, *Chem. Mater.*, 2014, **26**, 1485–1491.
25 N. Pellet, P. Gao, G. Gregori, T.-Y. Yang, M. K. Nazeeruddin, J. Maier and M. Grätzel, *Angew. Chem., Int. Ed.*, 2014, **53**, 3151–3157.
26 J.-W. Lee, D.-J. Seol, A.-N. Cho and N.-G. Park, *Adv. Mater.*, 2014, **26**, 4991–4998.
27 S. Hwang, H. Kwon, S. Chhajed, J. W. Byon, J. M. Baik, J. Im, S. H. Oh, H. W. Jang, S. J. Yoon and J. K. Kim, *Analyst*, 2013, **138**, 443–450.
28 Y.-P. Zhao, D.-X. Ye, G.-C. Wang and T.-M. Lu, *Proc. SPIE*, 2003, **5219**, 59–73.
29 H. Kwon, J. Ham, D. Y. Kim, S. J. Oh, S. Lee, S. H. Oh, E. F. Schubert, K.-G. Lim, T.-W. Lee, S. Kim, J.-L. Lee and J. K. Kim, *Adv. Energy Mater.*, 2014, **4**, 1301566.
30 M.-J. Kim, C.-R. Lee, W.-S. Jeong, J.-H. Im, T. I. Ryu and N.-G. Park, *J. Phys. Chem. C*, 2010, **114**, 19849–19852.
31 D. J. Poxson, F. W. Mont, M. F. Schubert, J. K. Kim and E. F. Schubert, *Appl. Phys. Lett.*, 2008, **93**, 101914.
32 S. H. Lee, J. Kwon, D. Y. Kim, K. Song, S. H. Oh, J. Cho, E. F. Schubert, J. H. Park and J. K. Kim, *Sol. Energy Mater. Sol. Cells*, 2014, **132**, 47–55.
33 S. H. Lee, H. Jin, D. Y. Kim, K. Song, S. H. Oh, S. Kim, E. F. Schubert and J. K. Kim, *Opt. Express*, 2014, **22**, A867–A879.
34 N. J. Cherepy, G. P. Smestad, M. Grätzel and J. Z. Zhang, *J. Phys. Chem. B*, 1997, **101**, 9342–9351.
35 W.-S. Jeong, J.-W. Lee, S. Jung, J. H. Yun and N.-G. Park, *Sol. Energy Mater. Sol. Cells*, 2011, **95**, 3419–3423.
36 N. Kopidakis, K. D. Benkstein, J. van de Lagemaat and A. J. Frank, *J. Phys. Chem. B*, 2003, **107**, 11307–11315.
37 H.-S. Kim and N.-G. Park, *J. Phys. Chem. Lett.*, 2014, **5**, 2927–2934.

